Proceedings of the 21st ICSMGE, Vienna, Austria, 14 – 19 June 2026. Pistrol, Adam & Schweiger (eds.)
Published by: ÖGG, Austrian Society for Geomechanics, Salzburg, Austria, ISBN 978-3-9503898-4-5
https://doi.org/10.53243/ICSMGE2026-993

Experimental investigation and modeling of Impact Stages during Dynamic Compaction

Benedict Löwe, Ralf Thiele
Institute of Geotechnics, UAS Leipzig, Germany, benedict.loewe@htwk-leipzig.de

Piotr Kanty
MENARD, Poland

Johannes Kirstein
MENARD, Germany

ABSTRACT: Dynamic compaction (DC) is a ground improvement method that densifies soils through the impact of heavy weights. While widely used, underlying physical mechanisms remain partially understood. This study presents a semi-analytical model for flat rigid-body penetration into dry sand, focusing on energy conversion and momentum transfer. Model tests with varied mass, velocity, and contact area were conducted using high-speed imaging and acceleration sensors. The analysis distinguishes two stages: an initial peak stage dominated by inertia and momentum transfer, followed by a plateau stage characterized by energy conversion through friction and damping. A time-dependent added mass, derived from momentum conservation, is introduced to model the soil–pounder interaction in the peak stage. The model reliably reproduces acceleration and crater depths, complementing empirical approaches with physical background. Results show that lower velocities and smaller contact areas promote deeper craters by preserving energy for the second stage. The model provides guidance for DC design and a framework for future studies, including effects wave propagation.

KEYWORDS: dynamic compaction, granular dynamics, added mass, momentum transfer, model test

1 INTRODUCTION

Dynamic compaction (DC) is a worldwide established method for cost-efficient and sustainable improvement of mixed to coarse-grained soils. The technique uses a heavy mass (pounder), that is dropped from great height using crawler cranes, impacting the ground to generate an impulse-like force. The impact reduces pore space and thereby increases the soils density. Consequently, both shear strength and stiffness improve, resulting in reduced and more uniform settlements, as well as increased resistance to shear failure. In practice, important influential parameters for controlling compaction effectiveness are the mass (m), impact velocity (v), and contact area (A) (Li et al. 2024). Based on extensive field tests, Menard & Broise first introduced the well-known empirical relation $DI = \sqrt{MH}$, describing the achievable depth of influence DI as a function of the potential energy of the pounder (Menard & Broise 1975). This formula built the foundation for numerous subsequent developments (e.g., Leonards 1980; Mayne et al. 1984; Mitchell 1981; Lukas 1995). Investigations using model tests (Li et al. 2024), field studies (Li et al. 2020), and numerical simulations (Gu & Lee 2002) fundamentally confirm the dependency on $\sqrt{E}$. However, Ghassemi (2009) indicates that DI tends to be overestimated at very high impact energies and may also depend on the contact area. This finding was also supported by others (Arslan et al. 2007). Subsequent studies consider not only energy $E = 0.5mv^2$ but also the momentum $p = m \cdot v$ of the pounder. Oshima & Takada (1997) argue that momentum is a better predictor for estimating the formation of the improved soil zone. Crater depth at the impact point has also been investigated in several studies as a function of momentum and energy. Models developed by Oshima & Takada (1997) and de Souza & Pasqual (2021) show the characteristic non-linear growth of crater depth with cumulative energy or momentum, which can typically be described using root or logarithmic functions. Scaled tests, however, often indicate underestimation at low and overestimation at high energy levels. Recent field and laboratory studies suggest that momentum may play a greater role in crater formation than energy (Knut et al. 2019). However, existing models are mostly empirical and offer limited physical explanation of the observed relationships. To better understand the pounder dynamics during penetration into sand, this work follows recent studies into mechanisms of dynamic compaction (e.g. Jia et al., 2021) and ballistics (e.g. Krizou & Clark 2020), analyzing short-term energy conversion during the impact using model tests. Focus is set on the dependencies on mass, velocity, and contact area. The aim is to develop an interpretable, semi-analytical model that highlights important physical aspects behind dynamic compaction and complements existing empirical models and theories.

2 MATERIALS AND METHODS

2.1 *Experimental Setup*

The model tests were conducted at a test rig developed for investigating DC at HTWK Leipzig (Figure 1). The experimental setup includes a test container (internal dimensions: 200 x 70 x 19.5 cm) with a transparent PMMA panel (80 × 60 cm), into which a pounder can be released from a height up to 2 m along guide rails. The drop height is continuously adjustable, with the pounder held at the desired position using an electromagnet.

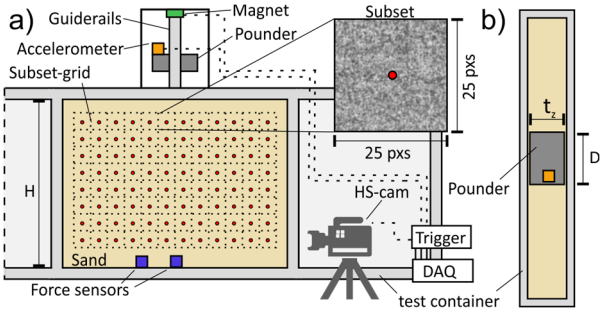

Figure 1. Schematic view of the experimental setup a) in-plane view and b) out-of-plane view.

The pounder is a flat-bottomed steel block with a square contact area (D × t_z). Its out-of-plane depth t_z is 19.2 cm, ensuring plane-strain conditions. To record the kinematics an acceleration sensor was mounted on the pounder (ASC

4511LN, ± 400 g). High-dynamic force sensors were placed at the bottom of the test container centrally (PCB LW59591, 450 N) and 30 cm off-center (PCB LW59544, 45 N). A high-speed camera (pco.dimax HD+) was used to capture the penetration process within the transparent field of view. All devices are connected to a data acquisition unit (DAQ). The release of the pounder is triggered using a remote-controlled mechanism that simultaneously starts all devices in synchronized time. Crater depths were measured using a laser distance meter and a ruler.

2.2 *Material and sample preparation*

Dry silica sand with a grain size distribution in the range of 0.015–2.015 mm was used as test material. The sand was poured into the test rig layer-wise using the air pluviation method and leveled to a uniform bed height of H = 0.6 m for each test. The movement of the pluviator is guided by linear actuators to ensure consistent speed and drop height. The thickness of each single layer was about 6 cm. Preliminary tests showed that this method results in no significant segregation of the material and produces a reproducible dry density of $\rho_d \approx 1.55$ g/cm³. To check the placement quality, each individual test included two measurements of the tip resistance using a cone-penetrometer (Eijkelkamp Penetrologger) outside the field of view. All tests showed identical initial tip resistance profiles, confirming uniform and reproducible material placement.

2.3 *Data Acquisition*

Acceleration and Force signals were recorded at a sampling frequency of 25 kHz. Camera images were captured at 1600 frames per second (fps) at a resolution of 1920 × 1440 pixels. The camera's exposure status was recorded simultaneously with the DAQ to ensure synchronized time stamps, allowing sensor and image data to be analyzed on a shared timeline.

2.4 *Test Procedure*

A total of 36 individual tests were conducted, with parameters mass, drop height, and pounder width varied in all possible combinations ($3^3 = 27$). The tests were scaled using a geometric factor of $\Pi = 15$, not to establish full dynamic similarity, but to demonstrate that the chosen combinations of mass, drop height, and contact area represent realistic proportions relative to full-scale dynamic compaction (see values in parentheses in Table 1). To ensure reproducibility, nine of the 36 tests (those with a width of 0.15 m) were repeated. No significant deviations were observed between the repeated trials. The following analysis therefore focuses on the 27 individual parameter variation tests.

Table 1: Parameters of the pounder used in the tests.

Parameter	low-level	mid-level	high-level
Mass m	7 kg (23.6 to)	10 kg (33.8 to)	13 kg (43.9 to)
Height h	0.2 m (3.0 m)	0.7 m (10.5 m)	1.2 m (18 m)
Width D	0.1 m (1.5m)	0.15 m (2.25 m)	0.2 m (3.0 m)

3 DATA ANALYSIS AND EVALUATION

3.1 *Sensor and DIC Signals*

The key quantities describing the pounder dynamics are acceleration, velocity, position, and mass. Velocity and position relative to the sand surface were obtained by double integrating the y-axis acceleration signal, assuming purely translational motion. To suppress high-frequency noise and drift, offset correction and a phase-neutral first-order Butterworth low-pass filter (1500 Hz, below the useful frequency) were applied. Numerical integration was performed using the trapezoidal rule. Comparable measurements from image data were derived via Digital Image Correlation (DIC) using GeoPIV (Stanier & White, 2013) in MATLAB with a subset size of 25 pixels. Images were preprocessed using Gaussian and CLAHE filters. Calibration was performed to correct for lens distortion and establish a measurement scale. To avoid random-walk effects, the GeoPIV-RG preconditioned optimization analysis scheme was used (Stanier et al., 2015). The resulting displacement fields were differentiated in time using a central difference scheme to obtain velocity and acceleration fields. As a result, each subset provides displacement, velocity and acceleration over time. Figure 2 shows a representative comparison between sensor and DIC measurements, with the DIC signal averaged over a 6 × 2 subset grid beneath the impact area.

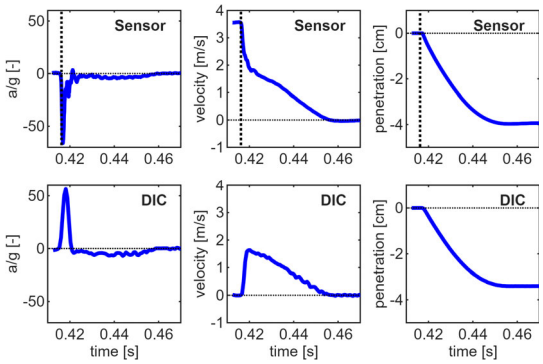

Figure 2. Kinematic quantities derived from sensor (left) and DIC (right) analysis. The vertical line indicates the beginning of impact.

Upon impact, a characteristic sudden increase in acceleration, known as the peak, occurs, which then rapidly decays and stabilizes on a plateau level (Knut 2023). In the peak region, the velocity of the pounder initially decreases significantly, during which only a small penetration depth is achieved. Most of the penetration occurs during the plateau, in which velocity decreases almost linearly. In contrast, the DIC results show initially inverse accelerations in the peak region, as the soil is first accelerated to its maximum velocity. In the subsequent plateau phase, the soil shows negative accelerations that closely follow those of the pounder, leading to an almost linear and simultaneous reduction in velocity. In this phase, the pounder and the soil directly beneath it move at nearly the same velocity, which is when most of the penetration occurs.

3.2 *Velocity Field Phenomenology (Example)*

To illustrate the soil motion beneath the pounder, Figure 3 shows an example of the buildup and collapse of a DIC velocity field. Clearly visible is a growing cone-shaped zone beneath the pounder, which is pushed into the soil as the pounder's velocity decreases. The velocity propagates in a wave-like form into more distant soil regions, where it is independent of the pounder's motion. The cone, referred to as a punching mechanism, is also described by Jia et al. (2018).

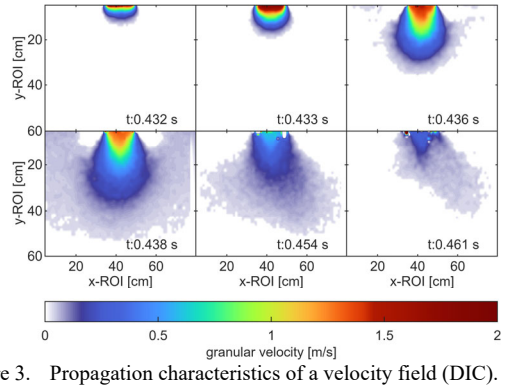

Figure 3. Propagation characteristics of a velocity field (DIC).

3.3 *Influence of Boundary Effects*

Due to the limited dimensions of the test container, wave reflections at the rigid boundaries of the test rig cannot be entirely avoided. The propagation velocity of the compression wave was determined from the peak travel time between the accelerometer on the pounder and the force sensors at the container base and is approximately 65 m/s. This corresponds to an arrival time of about 9–10 ms at the bottom and a return time of about 18–20 ms to the surface. Both events occur outside the peak. An inspection of the sensor and near-surface DIC signals at the calculated return time showed no anomalies (e.g., local maxima) that would indicate a significant presence of reflected waves. The negligible influence of the reflected wave on the pounder motion can be attributed to the strong attenuation of the stress amplitude during wave propagation. The maximum dynamic stress recorded by the force sensors at the container base is only 3–5 % of the maximum dynamic stress measured at the pounder. This strong attenuation behavior is consistent with the observations reported by Gu and Lee (2002), who found a comparable decrease in vertical stresses with increasing depth in their numerical back-analysis of 50 g centrifuge tests on medium-dense fine sand carried out by Thong (1994). In the present model tests, maximum dynamic boundary stresses of about 20 kPa were measured at the container base. This value is in the same range as the approximately 15 kPa reported by Li et al. (2024), for which no measurable influence on penetration behavior was observed. Together with the exponentially decreasing displacements observed from the surface to the base across all energy levels, these results indicate that the measurements and penetration behavior of the pounder are only weakly affected by the rigid bottom boundary due to the strong damping characteristics of the loosely deposited sand. This conclusion holds for to the single-blow tests presented in this study. For multiple blows in progressively compacted sand, however, the influence of the boundary conditions can be expected to increase.

4 SEMI-ANALYTICAL IMPACT MODEL

4.1 *Model Description and Equations*

Based on the sensor and DIC analyses carried out for all 27 tests, the penetration of the pounder into the soil can be divided into two stages. In the first stage ("peak"), the pounder's kinetic energy is mainly converted into kinetic energy of the soil directly beneath it. At the same time, a portion of the total momentum, proportional to energy loss, is transferred to the surrounding soil and propagates in a wave-like manner. In the second stage ("plateau"), the joint movement of the pounder and accelerated soil is continuously decelerated by internal reaction forces of the soil, converting and dissipating the remaining kinetic energy of the pounder. The resistance of granular media to penetration of a body can be described using Newton's second law of motion with the following force balance (Equation (1)). This approach is used in ballistic research and forms the basis for e.g. the Poncelet solution, which models projectile penetration into sand (Bless et al. 2015):

$$m_p \frac{dv}{dt} = F = m_p g - \alpha v^2 - \beta v - \gamma \qquad (1)$$

Where m_p denotes the projectile mass, v its instantaneous velocity, g gravitational acceleration, α inertial force, β damping and γ a frictional resistance. Equation (1) typically applies to pointed (conical) projectiles. To describe the penetration of a flat intruder into a non-Newtonian fluid, Waitukaitis & Jaeger (2012) proposed an extended model that adds a nonlinear inertia term to Equation (2). This model accounts for an added mass m_{add} that grows beneath the body during impact, increasing the deceleration of the penetrating body at high impact velocities significantly. Assuming an inelastic collision, the force balance becomes:

$$(m_p + m_{add}) \frac{dv}{dt} = - \frac{dm_{add}}{d_t} v + F_{ext} \qquad (2)$$

F_{ext} represents external forces acting on the body, including gravity (F_g = mg) and the fluid's buoyancy. Waitukaitis & Jaeger (2012) describe the growth of m_{add} geometrically as a fluid mass carried along with the penetrating object, depending on penetration depth and fluid properties. Aguilar & Goldman (2016) proposed a similar model to describe a robot foot's dynamics in granular media, also incorporating a term for m_{add} based on geometric considerations.

4.2 *Model Parameters*

4.2.1 *Added Mass*

The applicability of the models by Waitukaitis & Jaeger (2012) and Aguilar & Goldman (2016) to dynamic compaction was first evaluated. It was found that the geometric derivations used in these works for m_{add} did not yield satisfactory results for the experimental setup used in this study. This discrepancy is attributed to the different materials tested. Additionally, directly deriving m_{add} using the DIC acceleration field is problematic due to the difficulty in setting appropriate thresholds to isolate localized acceleration. Therefore, an alternative approach is proposed. This approach is based on the idealization introduced by Waitukaitis & Jaeger (2012), which assumes the penetration to be an inelastic collision. According to the definition of inelastic impact, total momentum is conserved. Since the pounder's momentum decreases due to deceleration, the total system mass must increase accordingly to conserve momentum. The time-dependent added mass m_{add} is defined as follows:

$$m_{add}(t) = \frac{p_{max}}{v_p(t)} - m_p \qquad (3)$$

Where p_{max} is the maximum momentum of the pounder, v_p its instantaneous velocity and m_p its mass. The assumption of momentum conservation immediately after contact was validated using synchronized sensor and DIC data analysis. Figure 4 shows the pounder's momentum (blue line) and the system's total momentum (red line). The total momentum is calculated as the sum of the pounder's momentum and the granular momentum (quasi-momentum in the sand), derived from the average DIC field velocity and the total mass within the DIC subset grid assuming a constant density. At the end of peak acceleration (gray line), the total momentum equals the pounder's maximum momentum. Beyond this point, momentum is transferred to undetectable regions, causing the measurable system momentum to decline. However, the total momentum is conserved with respect to the global system.

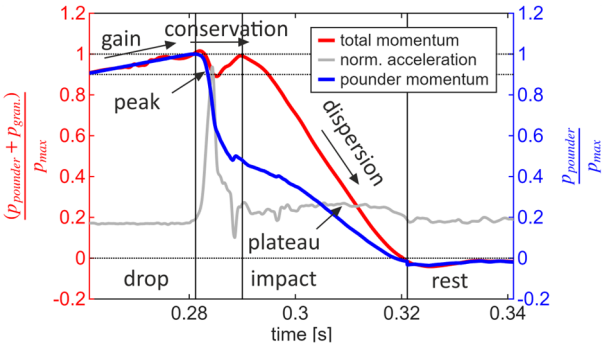

Figure 4. Comparison of pounder momentum and total momentum.

Based on momentum conservation, the maximum added mass ($m_{add,max}$) for all 27 tests was determined using the peak value from Equation (3). The end of the impact was defined as the moment when no further positive acceleration was detected in the soil, and the pounder and soil moved together as a single rigid body ($v_p = v_{sand}$). To incorporate $m_{add,max}$ into the mass term of Equation (2) for further analysis, it was modeled as a function of mass, area, and velocity using polynomial regression. The regression results show a strong correlation between these variables and the added mass (see Figure 5).

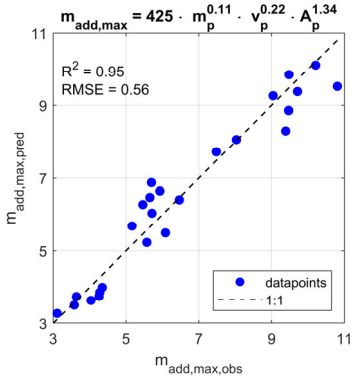

Figure 5. Observed (Eq.(3)) versus predicted (Eq. (4)) m_{add}.

The resulting regression model estimates $m_{add,max}$ as:

$$m_{add,max} = 425 * m_p^{0.1} * v_p^{0.2} * A_p^{1.3} \quad (4)$$

The time-dependent increase of m_{add} is approximated using a sigmoid function, reflecting the growth behavior observed in the results of Equation (4).

$$m_{add}(t) = \frac{m_{add,max}}{1 + \exp(-b * (t - T))} \quad (5)$$

Here, t denotes time, b the steepness of the growth, and T the time offset to reach the peak. The first time derivative of Equation (5), which enters Equation (2) as the m_{add} term, is:

$$\frac{dm_{add}}{dt} = \frac{m_{add,max} * b * \exp\left(-b * (t - T)\right)}{\left(1 + \exp\left(-b * (t - T)\right)\right)^2} \quad (6)$$

4.2.2 *Frictional Forces and Damping*

Waitukaitis & Jaeger and Aguilar & Goldman do not explicitly consider the effects of damping and friction in their models within the external force F_{ext}. However, other studies, such as Omidvar et al. (2012), indicate that these effects significantly influence the penetration behavior in sand. To capture these effects, the present model includes a friction term that varies with penetration depth and a damping term that depends on both depth and velocity.

The friction term is based on the approach by Kang et al. (2018), who modeled the quasi-static penetration of a body into sand using an Archimedean concept:

$$F_{fr} = K * \rho_d * g * V \quad (7)$$

Here, K is a dimensionless friction coefficient determined by the soil's internal friction angle φ, ρ_d is the dry bulk density of the soil, g is gravitational acceleration, and V denotes the volume of soil displaced during penetration, which increases with both penetration depth and contact area. For dry sand, Kang et. al (2018) reported K in the range of 110 - 120.

To investigate the influence of damping on plate penetration into sand, Gibson & Coyle (1968). conducted model tests. They proposed a model for the dynamic damping force related to the static penetration force, extended by empirical factors:

$$F_{dyn} = F_{static} * \frac{1}{v^n} * (u - 1) \quad (8)$$

Here, v denotes the instantaneous velocity of the pounder, n is an empirical exponent, F_{static} is the static frictional force equivalent to F_{fr} (Eq. (7)) and u is a soil-dependent empirical constant that characterizes the ratio of static to dynamic forces. For dry sand, u typically lies in the range 1.8 – 2.

5 MODEL RESULTS AND DISCUSSION

5.1 *Applied Model and Input Parameters*

Including the added mass (Eq. (4)) determined via momentum conservation, along with the previously defined effects of friction (Eq. (7)), damping (Eq. (8)), and gravity $F_g = (m_p + m_{add}) \cdot g$, the model used in this study takes the following form:

$$(m_p + m_{add})\frac{dv}{dt} = -\frac{dm_{add}}{d_t}v + F_{dyn} + F_{fr} + F_g \quad (9)$$

Fixed values of the parameters K, n, u, T and b (Table 2) were used in all simulations. The temporal development of m_{add} was defined by Equations (5) and (6). The pounder mass, initial velocity, and contact area served as the test-specific input parameters. The governing equation (9) was solved numerically in MATLAB using the built-in ODE45 solver.

Table 2: Added-Mass model parameters for simulation.

K [-]	n [-]	u [-]	T [s]	b [1/s]
50	0.2	1.9	0,002	2500

5.2 *Pounder Acceleration*

As shown in Figure 6, the temporal evolution of the measured acceleration signal (blue line) is well captured by the model (red line), with only a slight underestimation of the peak acceleration. The plateau acceleration, in contrast, does not show the small fluctuations present in the experimental data but matches well on average. Due to the high growth rates and the initially high velocity, the added-mass term causes the characteristic peak in acceleration. Damping and friction have little influence in this early stage, as both are depth dependent. After passing the peak, the growth rates of the added-mass term diminish. By this point, part of the momentum has already been transferred to the soil, and kinetic energy has been converted at the pounder. The remaining momentum and energy are primarily dissipated during the plateau stage through friction and damping, with the contribution of damping decreasing with velocity and that of friction increasing linearly with depth.

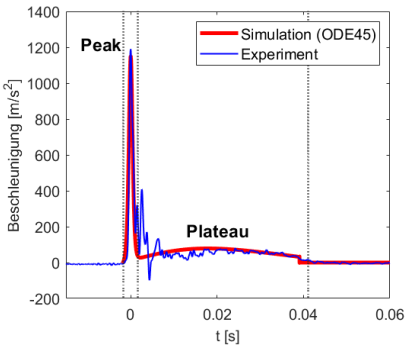

Figure 6. Simulated and experimental signal course.

Figure 7 compares simulated and experimental peak acceleration values from all 27 parameter variations. The linear regression (solid red line) indicates strong agreement, with a

slight tendency to underestimate the simulated peak acceleration with increasing peak acceleration. This behavior is consistent with the simulated signal course shown in Figure 6.

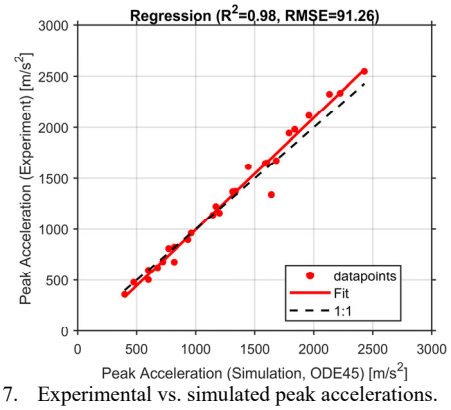

Figure 7. Experimental vs. simulated peak accelerations.

Figure 8 shows similar agreement for plateau accelerations between simulations and experimental data. For this comparison, plateau accelerations were averaged over time after $m_{add,max}$ was reached. Plateau acceleration is slightly underestimated at shallow penetration depths and slightly overestimated at greater depths. This suggests minor deviations of the test conditions from model assumptions regarding friction and damping, indicating the need for more precise tuning of the input parameters K, n, and u. Overall, the signal course, peak, and plateau accelerations show strong agreement with the experimental data, supporting the model assumptions.

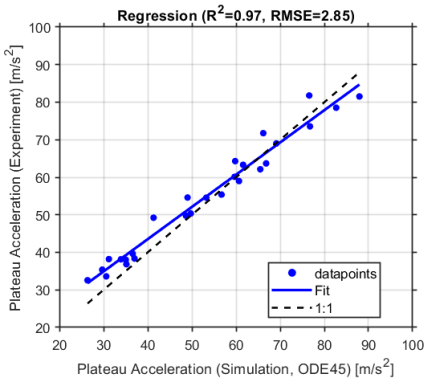

Figure 8. Experimental vs. simulated plateau accelerations.

5.3 *Crater Depth and Momentum Transfer*

From a practical perspective, the model's ability to predict penetration depth is of particular interest. Figure 9 presents a comparison between relative crater depths from the model tests and the simulations. The relative penetration is defined as the dimensionless ratio of crater depth to pounder width D:

$$relative\ Penetration = \frac{crater\ depth}{D} \qquad (10)$$

While the model exhibits strong overall accuracy in predicting relative penetration, it slightly overestimates penetration at shallow depths and underestimates it at greater depths, consistent with previously observed deviations in plateau acceleration. The significant influence of the contact area on crater formation is illustrated using different markers depending on the pounder width. It is evident that, at equal initial energy or momentum, smaller contact areas tend to result in greater penetration, i.e., crater depth.

The model attributes this behavior to distinct mechanisms during the peak and plateau stages. In the peak stage, the additional mass m_{add} s instantaneously accelerated. Under the assumed conservation of momentum, this produces a sudden momentum transfer from the pounder to m_{add}. As indicated by Equation (4), the magnitude of the forces involved in this transfer depends mainly on the contact area.

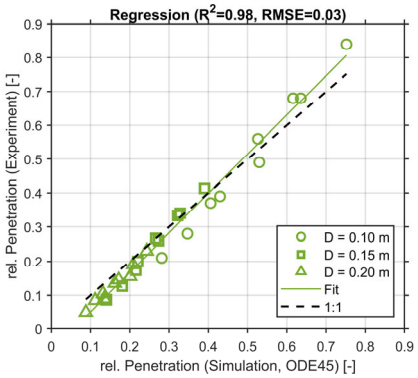

Figure 9. Experimental vs. simulated crater depths.

Equation (11) defines the momentum ratio as the ratio of momentum imparted to m_{add} after the peak stage to the initial total momentum p_{max}.

$$Momentum\ Ratio = \frac{p_{gran}}{p_{max}} = \frac{m_{add} * v_{sand,max}}{m_p * v_{p,max}} \qquad (11)$$

Figure 10 shows the agreement between experimental and simulated momentum ratio directly after peak stage. As the contact area increases, a larger proportion of the momentum is transferred to the soil, resulting in a stronger deceleration of the pounder. Consequently, less energy or momentum remains for crater formation during the plateau stage. Concurrently, larger contact areas displace more soil, leading to stronger frictional forces F_{fr} (Eq. (7)) as well as damping forces F_{dyn} (Eq. (8)). Hence, at equal initial momentum smaller contact areas must result in deeper craters because the velocity drop due to m_{add} is smaller, and the soil exerts lower total resistive forces.

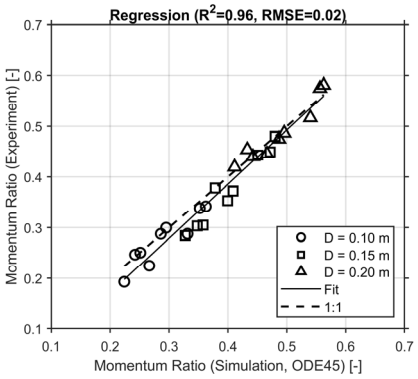

Figure 10. Experimental vs. simulated momentum ratio.

6 CONCLUSIONS

The article presents the development of a semi-analytical modeling approach for simulating the penetration of flat, rigid bodies into sand, based on interpretable and physically grounded relationships. The model relies on directly measurable input parameters (mass, initial velocity, area) as well as empirically derived parameters ($m_{add,max}$, K, n, u, T, and b). Among these, the first four show the greatest influence on the results of the simulation.

The incorporation of m_{add} follows Waitukaitis & Jaeger (2012) and Aguilar & Goldman (2016). However, in contrast to their methods, an alternative way is proposed here to determine m_{add} and its temporal evolution. This approach is based on the

principle of momentum conservation and can be derived from acceleration measurements at the pounder. The resulting maximum values obtained demonstrate that $m_{add,max}$ can be estimated as a function of mass, velocity, and contact area. Furthermore, a sigmoid-based model is introduced to describe the time-dependent evolution of m_{add}.

Comparison of the model predictions with experimental data demonstrates that the proposed model accurately captures both the peak and plateau accelerations. Moreover, the predicted penetration depths are in strong agreement with the experimentally measured crater depths. Based on the principles of energy conversion and momentum transfer outlined in the introduction, the following conclusions can be drawn:

1) The penetration process can be divided into two distinct stages. In Stage 1 (peak), rapid momentum transfer occurs from the pounder to the soil, converting the pounder's kinetic energy into motion of soil beneath the pounder. In Stage 2 (plateau), the remaining energy is mostly converted and dissipated through frictional and damping mechanisms. Notably, the contribution of Stage 2 to crater formation is disproportionately large compared to that of Stage 1 (Knut 2023).

2) The more energy that remains available during stage 2, the greater the resulting crater depth. A lower impact velocity and smaller contact area, as well as a higher pounder mass, tend to enhance crater formation. This is attributed to reduced momentum transfer during Stage 1, which preserves more energy at the pounder for crater formation in Stage 2. However, for a given total momentum, the contact area shows by far the most significant influence on crater depth.

3) Increasing the mass, rather than the velocity, appears to positively influence crater formation, as it does not directly affect the resistive forces (Eq. (7) + (8)) and has the least impact on m_{add} (Eq. (4)). This observation supports the hypothesis that crater depth may be more reliably predicted by momentum than by energy (Oshima & Takada 1997; Knut et al., 2019).

4) The intensity of wave propagation can be linked to the momentum transfer occurring in Stage 1 (Eq. (11)). A greater pounder mass, smaller contact area, and lower impact velocity reduce the momentum transfer and, consequently, the intensity. This aligns with practical observations (Li et al., 2023).

The proposed model extends existing DC theory by providing a physically interpretable framework for describing energy conversion and momentum transfer during impact. It also provides practical guidance for the design of compaction operations. However, the findings of this study are limited to dry sand under plane strain conditions. The presence of groundwater can significantly influence the relationships described and should be considered in future research. Additionally, the wave-like momentum propagation after stage 1 may contribute to deep soil compaction and should be investigated as a potential mechanism affecting the depth of influence (DI).

7 ACKNOWLEDGEMENTS

This work was funded by the Federal Ministry of Education and Research (BMBF), Federal Republic of Germany, under the project number 13FH160KX0.

8 REFERENCES

Aguilar, J. and Goldman, D.I. 2015. Robophysical study of jumping dynamics on granular media. *Nature Physics* 12(4), 278-283. doi:10.1038/nphys3568.

Arslan, H., Baykal, G. and Ertas, O. 2007. Influence of tamper weight shape on dynamic compaction, *Ground Improvement* 11(2), 61-66. doi:10.1680/grim.2007.11.2.61.

Bless, S., Omidvar, M. and Iskander, M. 2015. High-speed penetration of granular geomaterials, in Iskander et al. (eds.) Rapid Penetration into Granular Media. *Elsevier*, 93-144. doi:10.1016/B978-0-12-800868-3.00004-3.

de Souza, T.F. and Pasqual, R.P.S. 2021. New method to predict crater depth in dynamic compaction, *Geotechnical and Geological Engineering* 39(5), 3981–3993. doi:10.1007/s10706-021-01726-x.

Ghassemi, A., Pak, A. and Shahir, H. 2009. *Validity of Menard relation in dynamic compaction*. *Ground Improvement* 162(1), 37-45.

Gibson, G.C. and Coyle, H.M. 1968. Soil damping constants related to common soil properties in sands and clays. Research Report 125-1. Texas Transportation Institute, *Texas A&M University*, for U.S. DOT FHWA.

Gu, Q. and Lee, F.-H. 2002. Ground response to dynamic compaction of dry sand. *Géotechnique* 52(7), 481-493. doi:10.1680/geot.2002.52.7.481.

Jia, M. et al. 2018. PFC/FLAC coupled simulation of dynamic compaction. *Granular Matter* 20(4), Article 76. doi:10.1007/s10035-018-0841-y.

Jia, M. et al. 2021. Densification mechanism of granular soil under dynamic compaction. *Granular Matter* 23(3), Article 72. doi:10.1007/s10035-021-01136-z.

Kang, W. et al. 2018. Archimedes' law explains penetration of solids into granular media, *Nature Communications* 9, Article 1101. doi:10.1038/s41467-018-03344-3.

Knut, A. 2023. Influence of momentum and energy on the control and optimization of dynamic compaction. Doctoral thesis, *TU Dresden*.

Knut, A. et al. 2019. Influence of momentum and energy on dynamic compaction performance, in *Proc. XVII ECSMGE*, Reykjavík, EGS/IGS. doi:10.32075/17ECSMGE-2019-0487.

Krizou, N. and Clark, A.H. 2020. Power-law scaling of early-stage forces during granular impact. *Physical Review Letters* 124(17), 178002. doi:10.1103/PhysRevLett.124.178002.

Leonards, G.A., Cutter, W.A. and Holtz, R.D. 1980. Dynamic compaction of granular soils. *Journal of Geotechnical Engineering* 106(1), 35-44.

Li, P. et al. 2023. Parameters of dynamic compaction based on model test. *Soil Dynamics and Earthquake Engineering* 168, Article 107853. doi:10.1016/j.soildyn.2023.107853.

Li, X. et al. 2020. New method to evaluate strengthening efficiency in dynamic compaction. *International Journal of Geomechanics* 20(4), 04020024.

Li, X. et al. 2024. Experimental investigation into the effects of tamper weight and drop distance on dynamic soil compaction. *Acta Geotechnica* 19, 2563-2578. doi:10.1007/s11440-023-02198-4.

Lukas, R.G. 1995. Geotechnical Engineering Circular No. 1: Dynamic Compaction. *Federal Highway Administration*. FHWA-SA-95-037.

Mayne, P.W., Jones, J.S. and Dumas, J.C. 1984. Ground response to dynamic compaction, *Journal of Geotechnical Engineering*, 110(6). 757-773.

Menard, L. and Broise, Y. 1975. Theoretical and practical aspects of dynamic consolidation. *Géotechnique* 25(1), 3-18. doi:10.1680/geot.1975.25.1.3.

Mitchell, J.K. 1981. Soil improvement: state-of-the-art. *Proc. 10th ICSMFE*, Stockholm, Vol. 4, pp. 509-565.

Omidvar, M., Iskander, M. and Bless, S. 2012. Stress–strain behavior of sand at high strain rates. *International Journal of Impact Engineering*, 49, 192–213. doi:10.1016/j.ijimpeng.2012.03.004.

Oshima, A. and Takada, N. 1994. Effect of ram momentum on compaction by heavy tamping. *Proc. 13th ICSMFE*, New Delhi, 1141-1144.

Oshima, A. and Takada, N. 1997. Relation between compacted area and ram momentum. *Proc. 14th ICSMFE*, Vol. 3, 1641-1644.

Stanier, S.A. and White, D.J. 2013. Improved image-based deformation measurement for centrifuge applications. *Geotechnical Testing Journal* 36(6), 915-927. doi:10.1520/GTJ20130044.

Stanier, S.A. et al. 2015. Improved image-based deformation measurement for geotechnical applications. *Canadian Geotechnical Journal* 53(5), 727-739. doi:10.1139/cgj-2015-0253.

Thong, C.K. 1994. Propagation of shock waves in soil. BEng dissertation. National University of Singapore.

Waitukaitis, S.R. and Jaeger, H.M. 2012. Impact-activated solidification of dense suspensions via dynamic jamming fronts. *Nature* 487(7406), 205-209. doi:10.1038/nature11187.